Int. J. Heat Mass Transfer. Vol. 37, No. 1, pp. 43–52, 1994
Printed in Great Britain

0017–9310/94 $6.00 + 0.00

Heat transfer from a fully-developed pulsating flow in a curved pipe

JAE HWA CHUNG† and JAE MIN HYUN‡§

† Thermal Fluid Engineering Laboratory, Korea Institute of Science and Technology, P.O. Box 131, Cheong Ryang, Seoul, South Korea; ‡ Department of Mechanical Engineering, Korea Advanced Institute of Science and Technology, Yusong-ku, Taejon 305-701, South Korea

(*Received* 6 *January* 1993 *and in final form* 24 *June* 1993)

Abstract—Numerical studies are made of the flow and heat transfer characteristics of a fully-developed pulsating flow in a strongly curved pipe. Emphasis is placed on delineating the effects of the Reynolds number, and pulsation amplitude and frequency. By using a toroidal coordinate system, the complete, time-dependent incompressible Navier–Stokes equations are formulated. The peripherally-uniform temperature condition is imposed on the pipe wall. Particular attention is given to heat transfer properties over substantially extended parameter ranges of the Reynolds number Re and the Womersley number Wo. Use is made of a well-established numerical solution procedure, with minor amendments. The computed results on the flow field are in close agreement with the existing data in the overlapping parameter ranges. The spatial distributions of axial and secondary flows are depicted. The time variations of flow structure are displayed. The numerical results on the spatial and temporal variations of the thermal field are presented. The circumferential profiles of local Nusselt number are plotted at selected instants. When Wo is small, the time- and space-averaged Nusselt numbers, $\overline{Nu}_m$, is lower for a pulsating flow than for a corresponding non-pulsating flow. At moderate and high Wo, however, the difference in $\overline{Nu}_m$ between a pulsating and a non-pulsating flow is insignificant.

1. INTRODUCTION

IN RECENT years, much attention has been directed to the flow and heat transfer properties in a strongly-curved passageway. One prominent dynamic feature is the generation of secondary flow, which results mainly from the interplays between pressure gradient, centrifugal acceleration and viscous effects. The secondary flows tend to enhance overall convective heat transfer in a curved pipe in comparison to that in a straight pipe of comparable size. Several published accounts [1–3] highlight these significant technical issues in basic fluid dynamics. Also, an improved understanding of the physical process is vital to technological innovations of modern heat-exchangers.

The majority of previous investigations have dealt with steady-state flows. In many practical systems, however, the flow oftentimes contains appreciable pulsating components. Examples may be found in various curved-pipe heat exchangers attached to a reciprocating engine, Stirling-engine heat exchangers, to name a few [4, 5]. The pulsating components may be due to the inherent oscillatory characteristics of the system, or the pulsation is intentionally added to the flow with a view toward augmenting heat transports. These considerations warrant in-depth analyses of heat transfer properties of a pulsating flow in a curved pipe.

There has been a considerable body of literature on the dynamic aspects of a pulsating flow in a curved pipe. Lyne [6] carried out a theoretical investigation of a pure oscillating flow in a curved pipe of small curvature. Two distinguishable flow regimes were identified, and he showed the occurrence of an additional pair of secondary circulation in the inviscid core. This exhibited features which were different from the Dean-type vortices that were well known in non-pulsating flows. A theoretical study, under several restrictive assumptions, was initiated by Smith [7] for a pulsating flow. Some patterns of the secondary flows were visualized experimentally [8–10]. Talbot and Gong [11], by using a laser Doppler velocimeter to measure the secondary flows, experimentally confirmed the existence of a fully-developed region downstream of the inlet flow. In this region, the flow variables can be thought to be essentially independent of the axial position. Lin and Tarbell [12] computed the behavior of pulsating flow in a curved pipe, and parallel experimental observations were made, in limited parameter ranges, $2.5 \leqslant Wo < 5.5$, $Re < 1100$. Hamakiotes and Berger [13, 14] calculated the flow patterns in an extended Womersley number range ($7.5 < Wo < 25$). A numerical effort was undertaken by Tada *et al.* [15], in far more enlarged parameter spaces ($15.07 < De < 264.49$, $2.19 < Wo < 50.0$, $0.5 < k < 2.0$), which illustrated the flow structure in several characteristic regimes.

A literature survey reveals that research in the heat transfer characteristics of a pulsating flow in a curved

§ Author to whom correspondence should be addressed.

NOMENCLATURE

a	pipe radius
De	Dean number, $2Re(a/r_o)^{1/2}$
k	the pulsating amplitude ratio of axial velocity
Nu	the local Nusselt number at the wall
$\overline{Nu}_m$	the cycle- and peripherally-averaged Nusselt number
$\overline{Nu}_p$	the peripherally-averaged Nusselt number
p	nondimensional pressure
p^*	dimensional pressure
Pr	the Prandtl number, ν/κ
r	radial coordinate in the pipe cross section
r_o	dimensional mean radius of the curved region
Re	the Reynolds number, $w_m^* a/\nu$
t	nondimensional time
t^*	dimensional time
T	nondimensional temperature
T^*	dimensional temperature
T_b	nondimensional bulk temperature
T_w^*	dimensional wall temperature
u, v, w	nondimensional velocity components
u^*, v^*, w^*	dimensional velocity components
w_m^*	time-averaged, spatially-mean axial velocity
$\bar{W}$	the pulsating axial velocity averaged over the cross section
Wo	the Womersley number, $a(\omega/\nu)^{1/2}$.

Greek symbols

β	the coefficient of artificial compressibility
δ	the curvature ratio, a/r_o
θ	curve angle
κ	thermal diffusivity
ν	kinematic viscosity
ρ	density
τ	pseudo time
ϕ	angular coordinate in the pipe cross section
ω	the frequency of pulsation.

pipe is meager and incomplete. Simon *et al.* [16] employed a perturbation analysis to tackle heat transfer for very small Dean numbers. Rabadi *et al.* [17], by carrying out numerical calculations, pointed out inaccuracies of the above-stated perturbation analysis. However, the numerical endeavors of Rabadi *et al.* [17] were restricted to the case of one specific, relatively low, value of the Dean number ($De = 100.0$).

It is readily recognized that the global patterns of flow field and heat transfer properties in a curved pipe demonstrate substantial changes in character when appreciable magnitudes of pulsations are superimposed. The physical process crucially depends on several key nondimensional parameters. In order to acquire a systematic knowledge of the underlying phenomena, a comprehensive and organized parametric study is required. In the present paper, complete numerical solutions are sought to the unapproximated, time-dependent Navier–Stokes equations for a fully-developed pulsating flow in a curved pipe. The validity of the assumption of the fully-developed pulsating flow has been ascertained by previous experimental studies. For instance, Sumida *et al.* [10] considered a pipe curvature ratio of 1/7.6 and a pulsation amplitude of 1.0. In a similar effort, Talbot and Gong [11] dealt with the case of pipe curvature ratio of 1/7, and pulsation amplitude of 1.0. These prior investigations asserted that the pulsating flow attained a high degree of fully developed state at some downstream location along the axial length of the pipe. Clearly, the assumption of the fully-developed flow could become less accurate if the pulsation amplitude is very large for a strongly curved pipe. However, simulating a fully three-dimensional pulsating flow at the present stage poses a prohibitively expensive undertaking, although such endeavors are highly desirable in principle. Furthermore, the primary mission of the present work is to portray the effects of pulsation on the global heat transfer properties; the impacts of the axial variations of the flow variables constitute an issue of secondary importance. In summary, for the values of the parameters used in the present account, the assumption of the fully-developed state is a reasonable approximation, as can be inferred from the results of refs. [10, 11]. It is emphasized here that the ranges of both the Womersley number and the Reynolds number are enlarged considerably to cover large pulsation amplitudes and strong curvature ratios. The intention is to describe the major features of local as well as averaged heat transfer rates in the cross-sectional plane. The flow pulsation and the Reynolds number will be two principal dynamic effects that can be controlled externally.

The numerical solution methodologies have been well established. In the present study, some modifications were introduced, which made the calculations more adaptable to a pulsating flow in a curved pipe. These amended numerical procedures proved to be effective in securing the details of flow and thermal fields.

2. MATHEMATICAL FORMULATION

In accordance with the problem statement, a pulsating flow of an incompressible viscous fluid is maintained in a curved pipe of radius a. The radius of

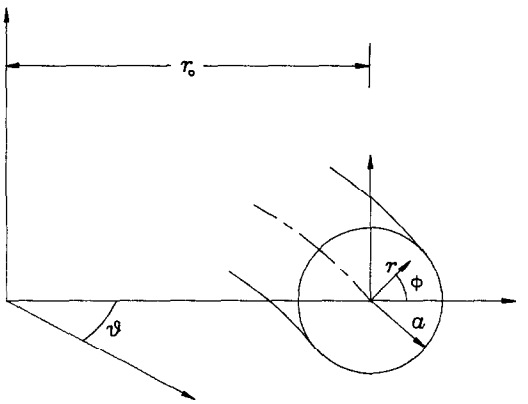

FIG. 1. Flow geometry and toroidal coordinate system.

curvature of the pipe is r_o. All the physical properties of the fluid are assumed to be constant (ν the kinematic viscosity, and κ the thermal diffusivity). As was shown by Lyne [6] and Rabadi *et al.* [17], the pulsating flow, with the pulsation frequency ω, is taken to be fully developed both in velocity and thermal fields. Following the methods used in Soh and Berger [18], a toroidal coordinate system (r, ϕ, θ), with the corresponding velocity components (u, v, w), is suitable for the present flow geometry. A schema of the flow configuration, with proper geometrical descriptions, is shown in Fig. 1.

The pulsating flow in the pipe is governed by the unsteady Navier–Stokes equations. Adopting standard notation, these equations, in dimensionless form, are expressed as

$$\frac{\partial}{\partial r}(rBu)+\frac{\partial}{\partial \phi}(Bv)=0 \tag{1}$$

$$St\frac{\partial u}{\partial t}+\frac{1}{rB}\left[\frac{\partial}{\partial r}(rBu^2)+\frac{\partial}{\partial \phi}(Buv)-Bv^2-\delta rw^2\cos\phi\right]$$
$$=-\frac{\partial p}{\partial r}+\frac{1}{Re}\left\{\frac{1}{rB}\left[\frac{\partial}{\partial r}\left(rB\frac{\partial u}{\partial r}\right)\right.\right.$$
$$\left.+\frac{\partial}{\partial \phi}\left(\frac{B\partial u}{r\partial \phi}\right)\right]-\frac{1}{r^2}\left(2\frac{\partial v}{\partial \phi}+u\right)$$
$$\left.+\frac{\delta v\sin\phi}{rB}+\frac{\delta^2\cos\phi}{B^2}(v\sin\phi-u\cos\phi)\right\} \tag{2}$$

$$St\frac{\partial v}{\partial t}+\frac{1}{rB}\left[\frac{\partial}{\partial r}(rBuv)+\frac{\partial}{\partial \phi}(Bv^2)+Buv+\delta rw^2\sin\phi\right]$$
$$=-\frac{1}{r}\frac{\partial p}{\partial \phi}+\frac{1}{Re}\left\{\frac{1}{rB}\left[\frac{\partial}{\partial r}\left(rB\frac{\partial u}{\partial r}\right)\right.\right.$$
$$\left.+\frac{\partial}{\partial \phi}\left(\frac{B\partial v}{r\partial \phi}\right)\right]+\frac{1}{r^2}\left(2\frac{\partial u}{\partial \phi}-v\right)-\frac{\delta u\sin\phi}{rB}$$
$$\left.-\frac{\delta^2\sin\phi}{B^2}(v\sin\phi-u\cos\phi)\right\} \tag{3}$$

$$St\frac{\partial w}{\partial t}+\frac{1}{rB}\left[\frac{\partial}{\partial r}(rBuw)+\frac{\partial}{\partial \phi}(Bvw)\right.$$
$$\left.+\delta rw(u\cos\phi-v\sin\phi)\right]$$
$$=-\frac{\delta}{B}\frac{\partial p}{\partial \theta}+\frac{1}{Re}\left\{\frac{1}{rB}\left[\frac{\partial}{\partial r}\left(rB\frac{\partial w}{\partial r}\right)\right.\right.$$
$$\left.\left.+\frac{\partial}{\partial \phi}\left(\frac{B\partial w}{r\partial \phi}\right)\right]-\frac{w\delta^2}{B^2}\right\} \tag{4}$$

$$St\frac{\partial T}{\partial t}+\frac{1}{rB}\left[\frac{\partial}{\partial r}(rBuT)+\frac{\partial}{\partial \phi}(BvT)-\frac{rw}{Pr}\right]$$
$$=\frac{1}{RePr}\frac{1}{rB}\left[\frac{\partial}{\partial r}\left(rB\frac{\partial T}{\partial r}\right)+\frac{\partial}{\partial \phi}\left(\frac{B\partial T}{r\partial \phi}\right)\right]. \tag{5}$$

In the above, the nondimensional quantities are related to the dimensional counterparts (indicated by asterisk) in the following fashion:

$$r=r^*/a,$$
$$(u,v,w)=(u^*,v^*,w^*)/w_m^*,$$
$$p=p^*/(\rho w_m^{*2}),$$
$$T=\frac{a(T_w^*-T^*)}{r_o\dfrac{\partial T^*}{\partial \theta}},$$
$$t=\omega t^* \tag{6}$$

in which w_m^* is the time-averaged, spatially-mean axial velocity of the mainstream over the cross-sectional plane. Compatible with the notion that only a fully-developed status is considered [17], the spatially-averaged axial gradient of fluid temperature, $\partial T^*/\partial\theta$, takes a constant value. In the present treatise, the wall temperature T_w^* is assumed to be independent of time and is uniform peripherally. In conformity with the aforementioned fully-developed flow assumption, T_w^* also varies linearly in the axial direction. The justification of the fully-developed flow was stated previously. In particular, the experimental evidence of refs. [10, 11] is relevant since the values of the parameters of these studies are comparable to those of the present work.

In the nondimensional governing equations (1)–(5), relevant dimensionless parameters emerge:

$Re \equiv w_m^* a/\nu$, the Reynolds number; $St \equiv a\omega/w_m^*$, the Strouhal number; $Pr \equiv \nu/\kappa$, the Prandtl number; $\delta \equiv a/r_o$, the curvature ratio; and $B \equiv 1+\delta r\cos\phi$.

From the above definitions, the Dean number $De \equiv 2Re(a/r_o)^{1/2}$, and the Womersley number $Wo \equiv a(\omega/\nu)^{1/2}$ are derived.

The boundary conditions at the pipe wall are

$$u=v=w=0, \quad T=0. \tag{7}$$

Due to the symmetry of pipe geometry, only one half of the pipe is considered in the numerical calculations. The symmetry conditions at the pipe center plane are

$$r = 0, \quad \frac{\partial u}{\partial \phi} = \frac{\partial w}{\partial \phi} = \frac{\partial T}{\partial \phi} = 0. \tag{8}$$

The pulsating axial velocity, averaged over the cross section, is specified as follows:

$$\bar{W} = 1 + k \cos t \tag{9}$$

where k indicates the nondimensional amplitude of pulsation. Upon integrating the w-momentum equation (4) over the cross section, the value of the corresponding pressure gradient in the axial direction, $\partial p/\partial \theta$, can be determined.

3. NUMERICAL PROCEDURE

The numerical techniques to solve the governing equations have been established by previous authors [18, 19]. In this section, only the highlights of numerical procedures will be briefly recapitulated.

The equations containing the time derivatives, equations (2)–(5), are rearranged, in vector form, as

$$St(\mathbf{V}^{n+1} - \mathbf{V}^n)/\Delta t + \nabla \cdot (\mathbf{V}^{n+1}\mathbf{V}^{n+1}) = -\nabla p^{n+1} - \frac{1}{Re}\nabla^2 \mathbf{V}^{n+1} = 0 \tag{10}$$

$$St(T^{n+1} - T^n)/\Delta t + \nabla \cdot (\mathbf{V}^{n+1}T^{n+1}) - \frac{1}{RePr}\nabla^2 T^{n+1} = 0 \tag{11}$$

in which $\mathbf{V}$ is the velocity vector, Δt the time increment, and indices n and $n+1$ refer to the time levels.

The continuity equation, expressing the divergence-free vector field, should be satisfied at every time step:

$$\nabla \cdot \mathbf{V}^{n+1} = 0. \tag{12}$$

To build effective computational schemes, the concept of pseudo-time, together with the introduction of the coefficient of artificial compressibility, is utilized. The idea of coefficient of artificial compressibility has been put forward in aerodynamic computational fields and its advantage has been documented [18]. With the use of these concepts, the time-advancing equations can be rewritten, in compact form, as

$$\partial H/\partial \tau + (\mathbf{A}_r + \mathbf{A}_\phi)\mathbf{H} + \mathbf{C}^v = 0 \tag{13}$$

and

$$\partial T/\partial \tau + (M + N)T + C^t = 0 \tag{14}$$

where τ indicates pseudo-time, and

$$\mathbf{H} = \begin{bmatrix} u \\ v \\ w \\ p \end{bmatrix},$$

$$\mathbf{A}_r = \begin{bmatrix} M & 0 & 0 & \dfrac{\partial}{\partial r} \\ 0 & M & 0 & 0 \\ 0 & 0 & M & 0 \\ \dfrac{1}{\beta r}\dfrac{\partial}{B\partial r}(rB\cdot) & 0 & 0 & 0 \end{bmatrix},$$

$$\mathbf{A}_\phi = \begin{bmatrix} N & 0 & 0 & 0 \\ 0 & N & 0 & \dfrac{\partial}{r\partial \phi} \\ 0 & 0 & N & M \\ 0 & \dfrac{1}{\beta r}\dfrac{\partial}{B\partial \phi}(B\cdot) & 0 & 0 \end{bmatrix},$$

$$\mathbf{C}^v = \begin{bmatrix} -v^2/r - \delta \cos\phi(w^2/B) + \{(2\partial v/\partial \phi + u)/r^2 - \delta v \sin\phi/B + \delta^2 \cos\phi(u\cos\phi - v\sin\phi)/B^2\}/Re + \sigma(u - u^n) \\ uv/r + \delta w^2 \sin\phi/B + \{(2\partial u/\partial \phi - v)/r^2 + \sigma(v - v^n) + \delta u \sin\phi/rB - \delta^2 \sin\phi(u\cos\phi - v\sin\phi)/B^2\}/Re \\ \delta rw(u\cos\phi - v\sin\phi)/B + \delta(\partial p/\partial \theta)/B + (\partial^2 w/B^2)/Re + \sigma(w - w^n) \\ 0 \end{bmatrix},$$

$$C^t = -(w/B)/Pr + \sigma(T - T^n),$$

$$M = \frac{1}{rB}\left\{\frac{\partial}{\partial r}(rBu\cdot) - \frac{1}{Re}\frac{\partial}{\partial r}\left(rB\frac{\partial \cdot}{\partial r}\right)\right\},$$

$$N = \frac{1}{rB}\left\{\frac{\partial}{\partial \phi}(Bv\cdot) - \frac{1}{Re}\frac{\partial}{\partial r}\left(B\frac{\partial \cdot}{r\partial r}\right)\right\},$$

$$\sigma = St/\Delta t.$$

The central differencing in the staggered grid network is adopted for the advection and diffusion terms. The general solution procedures are similar to those expounded in [18]. Minor differences are that, in the present formulation, the unsteady terms are incorporated into the source terms, $\mathbf{C}^v$ and C^t. In order to facilitate convergence in pseudo-time τ, a factored ADI finite-difference technique was used. This leads to triangular matrices for both the r and ϕ equations, which are amenable to the Thomas algorithm [20]. The geometrical center of the pipe ($r = 0$) represents a mathematical singular point. For the treatment of the center, the numerical approximation method of ref. [18] was selected. At each time step, the fully converged solutions for the velocity fields are obtained first, and based on these, the temperature field is secured.

The grid points were typically (20×20) for low Reynolds numbers, and (24×30) for high Reynolds numbers. The mesh network was stretched to cluster the grid points near the wall. In the actual computations, the integration of the governing equations was performed over a number of pulsation cycles until

the periodicity of the results was attained. The computational time interval Δt was chosen such that 360 or 720 time steps, depending on the values of the relevant parameters, constituted a pulsation cycle. Typically, these imply that the nondimensional time interval is $2\pi/360$ or $2\pi/720$. Normally, approximately 20 iterations were required to reach the prescribed accuracy (10^{-4} in the present study) in the velocity and temperature fields at each time level. Usually, about 6–10 pulsation cycles were needed for the computed solution to approach a periodic status; however, at high Womersley numbers Wo, the periodicity of solutions was realized after more pulsation cycles were encompassed. The tests of grid-convergence and time step sensitivity were performed for several exemplary calculations. The results were generally satisfactory, providing credence to the use of the mesh network and time interval selected in this study.

4. RESULTS AND DISCUSSION

As stressed previously, this study aims to acquire comprehensive flow and heat transfer data over wide ranges of the externally specifiable parameters. To this end, the two principal parameters were set: the Reynolds number, $Re = 50$, 200, 400, and the Womersley number, $Wo = 2.5$, 5.0, 7.5, 10.0, 15.0, and 20.0. These clearly represent vastly extended parameter spaces over the prior investigations. In parallel with the preceding numerical examinations [13, 14, 17], discussions will be concentrated for the computations using the Prandtl number $Pr = 0.7$, the pulsation amplitude $k = 1.0$, and the pipe curvature ratio $\delta = 1/7$. However, additional calculations were obtained for $Pr = 5.0$ and for $k = 0.5$, which illustrated the effects of Pr and of k.

4.1. *The velocity field*

In the first, it is useful to appreciate the general interrelation between the cross sectional area-averaged axial velocity $\bar{W}$, expressed in (9), and the axial pressure gradient $\partial p/\partial\theta$, which drives the axial flow. The results in Fig. 2 are prototypical of the time-dependent variations of these two physical quantities. The shape of $\bar{W}$ is assumed to be a simple sinusoidal function, shown in Fig. 2(a). When Wo is small (say, $Wo = 2.5$), the axial pressure gradient $\partial p/\partial\theta$ is nearly in phase with $\bar{W}$. This implies that the overall situation is akin to a quasi-steady process. The axial velocity $\bar{W}$ responds to the instantaneous value of pressure gradient when the pulsation frequency is very low. On the other limit, when Wo is large, the magnitude of $\partial p/\partial\theta$ is amplified substantially. This finding is consistent with the earlier reports [13, 14]. It is also notable that the phase difference between $\bar{W}$ and $\partial p/\partial\theta$ approaches $\pi/2$ at large Wo. As can be deduced from the momentum equation (4), at high pulsation frequencies, the dominant balance is between the unsteady term and the axial pressure gradient. The above observations on the temporal behavior of $\bar{W}$ and $\partial p/\partial\theta$ are in broad agreement with the detailed theoretical examinations of the pulsating flow in a curved pipe [21].

The local distributions of instantaneous axial velocity w and the vector plots of secondary flows are exhibited in Figs. 3 and 4. The velocity profiles are illustrated at four different instants in reference to Fig. 2(a): $t = 0$ and $t = \pi$ correspond, respectively, to the instants of maximum $\bar{W}$ and minimum $\bar{W}$; $t = \pi/2$ and $t = 3\pi/2$ are the respective instants of maximum negative $\partial\bar{W}/\partial t$ and maximum positive $\partial\bar{W}/\partial t$.

The local profiles of w display considerably different patterns, depending on the value of Wo and Re. In general, for small Wo, the spatial gradients of w are less pronounced near the inner wall than the outer wall. However, at large Wo, the spatial variations of w near the inner wall are comparable in magnitude with those near the outer wall. Furthermore, at large Wo, the flow demonstrates rapid spatial variations in the wall regions. As illustrated in Fig. 2, the temporal fluctuation of axial pressure gradient is substantial when the pulsation frequency is large. Due to the viscosity effect, the fluid particles in the wall regions

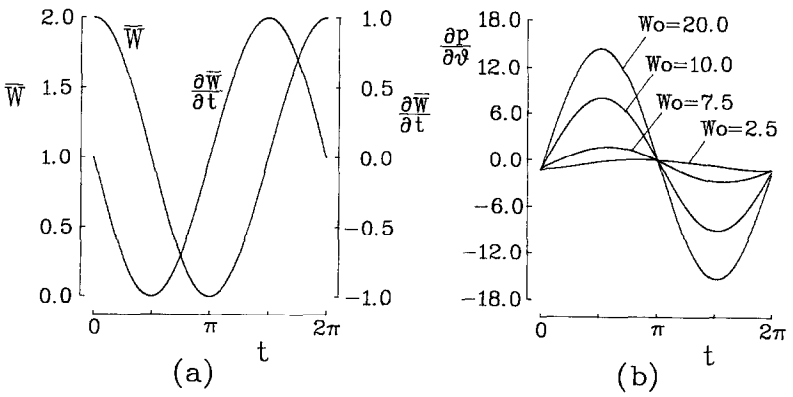

FIG. 2. Temporal behavior of flow variables. $Re = 200$, $k = 1.0$. (a) $\bar{W}$ and $\partial\bar{W}/\partial t$, (b) computed results of $\partial p/\partial\theta$.

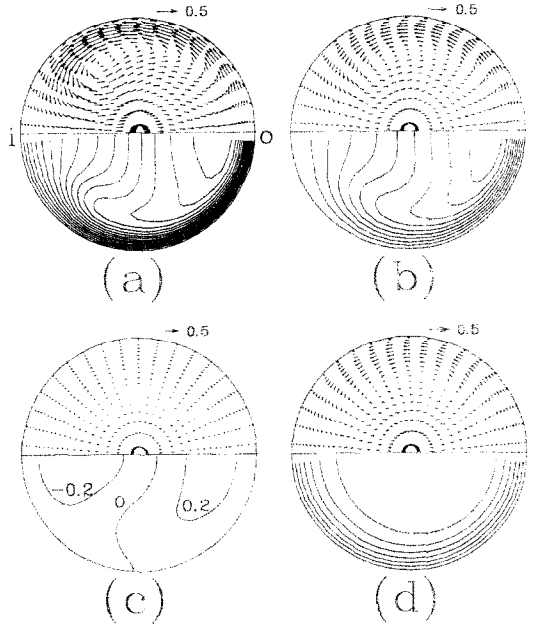

FIG. 3. Vector plots of secondary flows (the upper hemisphere), and contours of axial velocity w (the lower hemisphere). $Re = 200$, $Wo = 5.0$, $k = 1.0$. Times are (a) $t = 0.0$, (b) $t = \pi/2$, (c) $t = \pi$, (d) $t = 3\pi/2$. The values of iso-velocity contour lines are, from the outer to the inner wall, 0.2, 0.4, 0.6, 0.8, 1.0, 1.2, 1.4, 1.6, 2.6, 2.8 and 3.0.

will have smaller inertia than those in the interior core region. Consequently, the fluids near the walls would respond more readily to the prevailing axial pressure gradient, and this process is more conspicuous at large

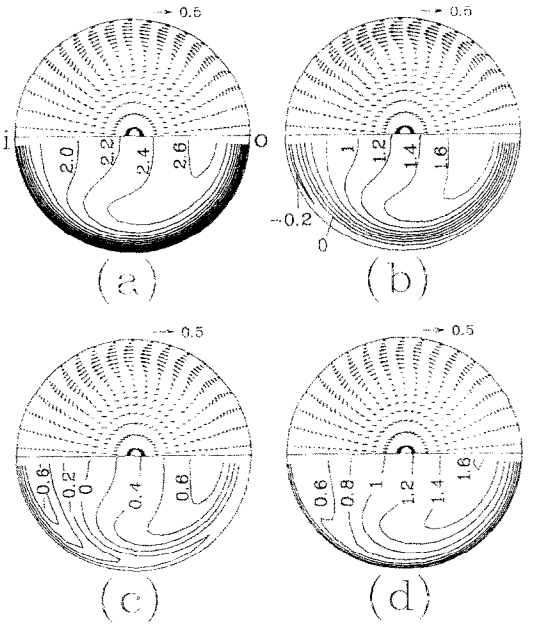

FIG. 4. Vector plots of secondary flows (the upper hemisphere), and contours of axial velocity w (the lower hemisphere). $Re = 200$, $Wo = 20.0$, $k = 1.0$. Times are (a) $t = 0.0$, (b) $t = \pi/2$, (c) $t = \pi$, (d) $t = 3\pi/2$. The values of iso-velocity contour lines are, from the outer to the inner wall, 0.2, 0.4, 0.6, 0.8, 1.0, 1.2, 1.4, 1.6, 1.8, 2.0, 2.2, 2.4 and 2.6.

Wo. It is also interesting to point out the existence of localized reverse flow ($w < 0$) near the inner wall region when the overall axial velocity $\bar{W}$ is very small (near $t = \pi$ as shown in Figs. 3 and 4). The general descriptions of axial flow profiles, as presented in Figs. 2–4, are in broad qualitative consistency with the available experimental and numerical data [21, 22]. No direct quantitative comparisons have been attempted since the precise values of the principal nondimensional parameters of these prior studies were at variance.

Next, the fields of secondary flows are inspected. First, the case of a low Wo is considered. In the initial phase of negative $\partial\bar{W}/\partial t$ (near $t = 0$), the secondary flows are intensified in the areas close to the pipe periphery, and they are directed mostly from the outer wall region to the inner wall region. It is recalled that the axial flows are also vigorous at this stage. At the time instants when $\partial\bar{W}/\partial t$ changes sign (near $t = \pi$), $\bar{W}$ is minimum, and the secondary flows weaken. Notice that localized reverse flows appear in this phase. At the instants when $\bar{W}$ is accelerated (near $t = 3\pi/2$), both the axial flow and secondary flows are strengthened. As can be seen in Fig. 4, at a large value of Wo, the concentration of the gradients of w near the pipe wall periphery is discernible. However, the overall time variation of both axial and secondary flows at large Wo tend to be milder than at low Wo.

4.2. *The temperature field*

The numerical results of temperature field and attendant heat transfer characteristics will now be presented.

The isothermal contour lines are exhibited in Figs. 5 and 6. For the case of low Wo (see Figs. 5(a) and 6(a)), large spatial temperature gradients are notable near the outer wall periphery regions at time instants ranging from $t = 0$ to $\pi/2$. This represents intense convective activities, associated with large values of w in the outer wall region, and this leads to higher heat transports. Expectedly, this trend is more discernible as Re increases. At a time when the axial velocity assumes a very low value (see the plots at $t = \pi$), convective activities diminish and, consequently, the overall spatial temperature gradients throughout the pipe cross section are very small. As $\bar{W}$ increases (see the plots at $t = 3\pi/2$), the spatial temperature gradients gain in magnitude. For the case of high Wo (see Figs. 5(b) and 6(b)), the temporal variations of thermal fields are insignificant. Furthermore, at any given instant, the global spatial gradients of temperature are much milder than for low Wo. The intensification of temperature gradients in the outer wall region is seen to be more noticeable as Re increases, which is qualitatively similar to the results for low Wo.

In order to introduce physically meaningful Nusselt numbers, the fluid bulk temperature $\bar{T}_b$, properly averaged in time and space, is defined, in a manner similar to [16]:

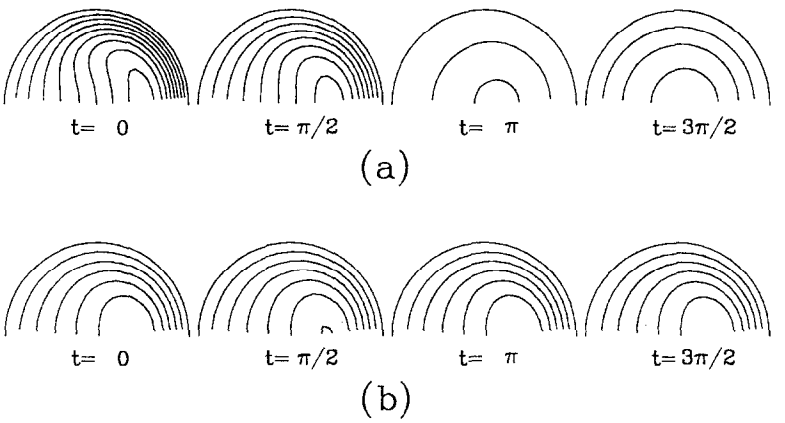

FIG. 5. Plots of isotherms. $Re = 50, k = 1.0, Pr = 0.7$. (a) $Wo = 2.5$, (b) $Wo = 20.0$. The values of isotherm contour lines are, from the outer to the inner wall, 2.5, 5.0, 7.5, 10.0, 12.5, 15.0, 17.5 and 20.0.

$$\bar{T}_b = \frac{\int_0^{2\pi}\int_0^{2\pi}\int_0^1 wTr\,dr\,d\phi\,dt}{\int_0^{2\pi}\int_0^{2\pi}\int_0^1 wr\,dr\,d\phi\,dt}.$$

The local Nusselt number Nu is now defined using the bulk temperature $\bar{T}_b$ as [16]

$$Nu = -\frac{2}{\bar{T}_b}\left(\frac{\partial T}{\partial r}\right)_{r=1}.$$

It follows that the peripherally averaged Nusselt number $\overline{Nu}_p$ is

$$\overline{Nu}_p = \frac{1}{2\pi}\int_0^{2\pi} Nu(1+\delta\cos\phi)\,d\phi,$$

and the cycle-averaged and peripherally-averaged Nusselt number $\overline{Nu}_m$ is

$$\overline{Nu}_m = \frac{1}{2\pi}\int_0^{2\pi} \overline{Nu}_p\,dt.$$

The temporal and peripheral variations of the local Nusselt number Nu are analyzed in Figs. 7–9. A clear finding emerges that Nu increases fairly monotonically as the peripheral angle ϕ moves from π (corresponding to the inner wall) to 0 (corresponding to the outer wall). Higher rates of heat transfer in the regions near the outer wall are the results of enhanced convective activities, with increased axial velocities, owing to the curvature effect of a curved pipe. As Re increases, the peripheral variations of Nu are more pronounced. As indicated in Fig. 9, at a large value of Re, the localized heat transfer augmentation near the outer wall is substantial. When Wo is low, the temporal variations of Nu are generally appreciable, and these trends are particularly noticeable near the outer wall. As Wo increases, the temporal changes of Nu tend to be small.

Re-plotting the numerical data, the behavior of $\overline{Nu}_p$ is examined in further detail. When Re is low (see Fig. 10(a)), the magnitudes of temporal variations of $\overline{Nu}_p$ are smaller than for high Re (see Fig. 10(b)). The overall augmentation of heat transport at higher values of Re is discernible in Fig. 10 as well. For a

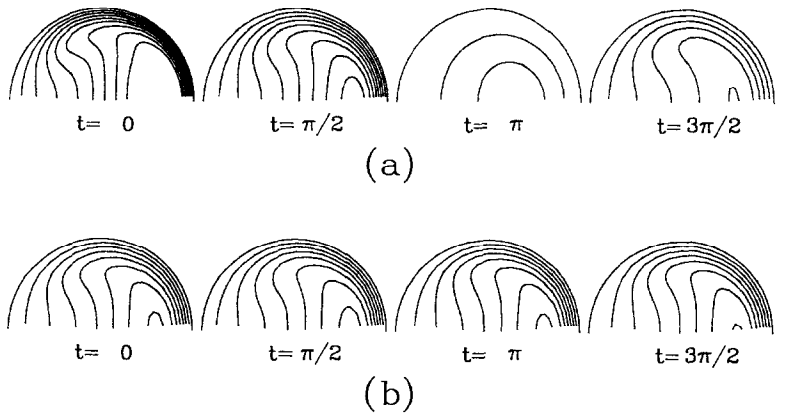

FIG. 6. Plots of isotherms. $Re = 200, k = 1.0, Pr = 0.7$. (a) $Wo = 2.5$, (b) $Wo = 20.0$. The values of isotherm contour lines are, from the outer to the inner wall, 5.0, 10.0, 15.0, 20.0, 25.0, 30.0, 35.0 and 40.0.

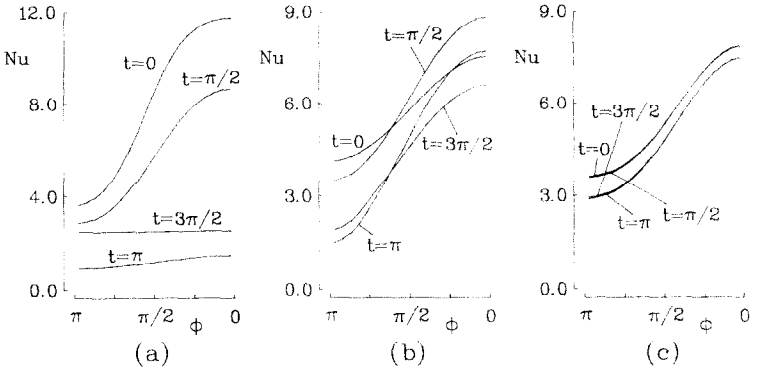

FIG. 7. The peripheral profiles of Nu. $Re = 50$, $k = 1.0$, $Pr = 0.7$. (a) $Wo = 2.5$. (b) $Wo = 7.5$. (c) $Wo = 20.0$.

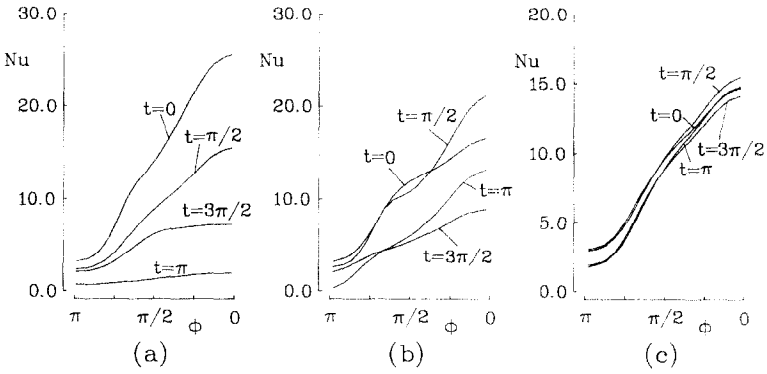

FIG. 8. The peripheral profiles of Nu. $Re = 200$, $k = 1.0$, $Pr = 0.7$. (a) $Wo = 2.5$. (b) $Wo = 7.5$. (c) $Wo = 20.0$.

fixed value of Re, the temporal changes of $\overline{Nu}_p$ are far more prominent at low values of Wo. Cross-referencing the $\bar{W}$-profile of Fig. 2 and the $\overline{Nu}_p$-profiles of Fig. 10 discloses the phase relations between these two physical quantities. When Wo is low, $\bar{W}$ and $\overline{Nu}_p$ are nearly in phase. However, at large Wo, the phase lag between $\bar{W}$ and $\overline{Nu}_p$ tends to increase.

Calculations were performed to gauge the effects of the Prandtl number Pr and the magnitude of the pulsation amplitude k. Typical results are displayed in Fig. 11. As is discernible in Fig. 11(a), the convective heat transfer, as reflected in $\overline{Nu}_p$, is substantially enhanced for $Pr = 5.0$ in comparison to $Pr = 0.7$. However, the phase lag of $\overline{Nu}_p$ is affected slightly by the variation in Pr. The impact of k, as displayed in Fig. 11(b), is consistent with the intuition. The time evolution of $\overline{Nu}_p$ tends to be amplified as k increases.

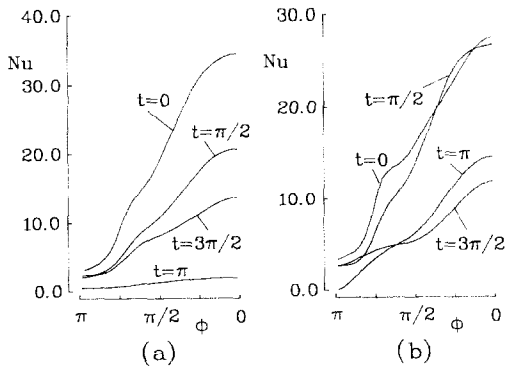

FIG. 9. The peripheral profiles of Nu. $Re = 400$, $k = 1.0$, $Pr = 0.7$. (a) $Wo = 2.5$, (b) $Wo = 7.5$.

Finally, the global heat transport characteristics are best reflected in the behavior of $\overline{Nu}_m$. Figure 12 summarizes the results of entire numerical computations. For the purpose of comparisons, the Nusselt numbers were re-calculated for given values of Re of non-pulsating flows (by setting $k = 0$ in equation (9)). These exercises will bring into focus the alterations in global heat transfer caused by the addition of pulsating components. The computed $\overline{Nu}_m$ results for non-pulsating flows are in close agreement with the existing data in the literature [23]. An obvious finding that emerges from Fig. 12 is that, at low and moderate values of Wo, $\overline{Nu}_m$ for a pulsating flow tends to be lower than that for a non-pulsating flow, and at high Wo, not many changes are seen in $\overline{Nu}_m$ by the presence of pulsations. This tendency of decrease in global heat transports in a pulsating flow was also

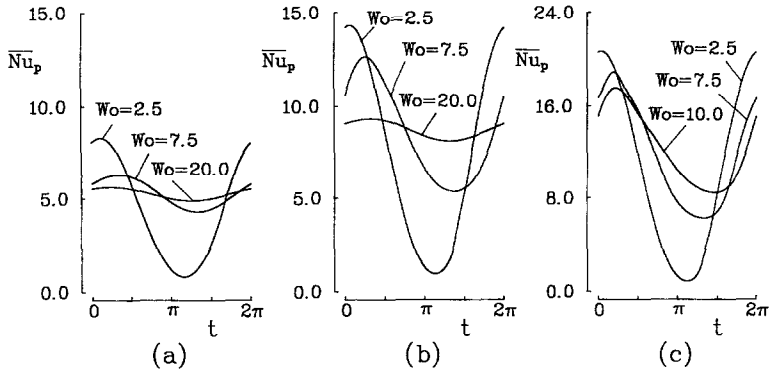

FIG. 10. Temporal variation of peripherally-averaged Nusselt number $\overline{Nu}_p$ with Re. $k = 1.0$, $Pr = 0.7$. (a) $Re = 50$, (b) $Re = 200$, (c) $Re = 400$.

noted in ref. [17] for one specific low value of the Dean number.

The above observations on $\overline{Nu}_m$ need careful interpretation. Note that the concept of Nu here is strictly applicable to the heat transport between the pipe wall and the fluid. Oftentimes, the claim of heat transfer enhancement by the addition of pulsations, as reported in the literature [4, 24], is concerned with heat transport between the fluids in the upstream and the fluids in the downstream locations. Also, it should be pointed out that, in the present treatment, a fully-developed flow is assumed, and the condition of the peripherally-uniform temperature at the pipe wall is enforced.

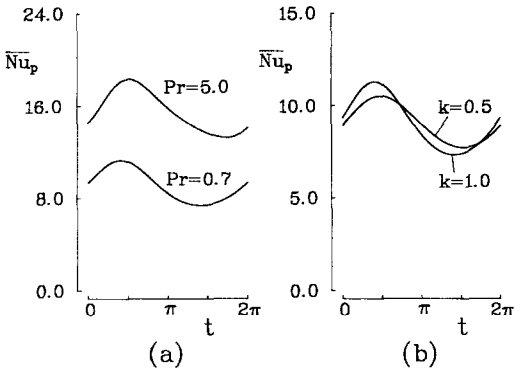

FIG. 11. Temporal variation of peripherally-averaged Nusselt number $\overline{Nu}_p$ with Pr and k. $Re = 200$, $Wo = 10.0$. (a) Effect of Pr, $k = 1.0$, (b) effect of k, $Pr = 0.7$.

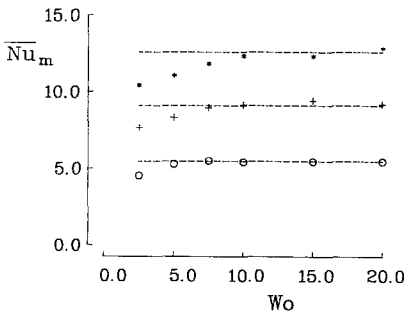

FIG. 12. The numerical results of $\overline{Nu}_m$. $k = 1.0$, $Pr = 0.7$. The broken lines indicate the values for the corresponding non-pulsating flows ($k = 0.0$ in equation (9)). ○ $Re = 50$; + $Re = 200$; * $Re = 400$.

5. CONCLUSION

The computed results reveal the flow and thermal fields over a wide range of Re, as they are affected by pulsations of varying frequencies. The present computational studies are concerned with the case when the pulsation amplitude is substantial and the pipe curvature is strong. The results are consistent with the preceding flow data of the literature in the overlapping parameter ranges.

The local axial velocity field displays large gradients in the wall peripheral area, and the velocity gradients are more pronounced near the outer wall. The concentration of axial velocity gradients in the wall regions intensifies as the Womersley number Wo increases. It is noted that localized reverse flow zones appear in the inner wall areas when the mean axial speed $\bar{W}$ takes low values. These tendencies become more discernible as Re increases. When Wo is low, the secondary flows exhibit strong temporal variations. The major parts of the secondary flows are seen near the peripheral areas, and they are oriented in the circumferential direction, moving from the outer to inner wall. At high values of Wo, the temporal variations of secondary flows are weak.

Analyses were made of the detailed patterns of isotherms. In general, the temperature gradients are large in the peripheral regions, and these are particularly noticeable near the outer wall. Concentration of the temperature gradients near the peripheral areas is more pronounced as Re increases. For a given value of Re, the temporal variations of the temperature fields are more prominent at low values of Wo.

The computed results of the time- and space-averaged Nusselt number, $\overline{Nu}_m$, indicate that $\overline{Nu}_m$ of a pulsating flow is lower than that of non-pulsating flow, when Wo is low. At large Wo, the differences in

$\overline{Nu}_m$ between a pulsating and a non-pulsating flow diminish.

Acknowledgements—Appreciation is extended to the referee whose constructive comments led to improvements in the paper. This work was supported in part by research grants from the Ministry of Science and Technology, Korea.

REFERENCES

1. W. R. Dean, Note on the motion of fluid in a curved pipe, *J. Phil. Mag.* **20**(7), 208–223 (1927).
2. S. A. Berger, L. Talbot and L. S. Yao, Flow in curved pipes, *Ann. Rev. Fluid Mech.* **15**, 461–512 (1983).
3. H. Ito, Flow in curved pipes, *JSME Int. J.* **30**, 543–552 (1987).
4. M. F. Hwang and A. Dybbs, Heat transfer in a tube with oscillatory flow, ASME paper 83-WA/HT-90, 1–12 (1983).
5. T. W. Simon and J. R. Seume, A survey of oscillating flow in Stirling engine heat exchanger, *NASA Report* No. 182108 (1988).
6. W. H. Lyne, Unsteady viscous flow in a curved pipe, *J. Fluid Mech.* **45**, 13–31 (1971).
7. F. T. Smith, Pulsatile flow in curved pipes, *J. Fluid Mech.* **71**, 15–42 (1975).
8. B. R. Munson, Experimental results for oscillating flow in a curved pipe, *Phys. Fluids* **18**, 1607–1609 (1975).
9. A. F. Bertelsen, An experimental investigation of low Reynolds number secondary streaming effects associated with an oscillating viscous flow in a curved pipe, *J. Fluid Mech.* **70**, 519–527 (1975).
10. M. Sumida, K. Sudou and H. Wada, Pulsating flow in curved pipes (4th Report, Secondary flow), *Trans. J.S.M.E.* **54**(505), 2375–2381 (1988) (in Japanese).
11. L. Talbot and K. O. Gong, Pulsatile entrance flow in a curved pipe, *J. Fluid Mech.* **127**, 1–25 (1983).
12. J. Y. Lin and J. M. Tarbell, An experimental and numerical study of periodic flow in a curved pipe, *J. Fluid Mech.* **100**, 623 (1980).
13. C. C. Hamakiotes and S. A. Berger, Fully developed pulsatile flow in a curved pipe, *J. Fluid Mech.* **195**, 23–55 (1988).
14. C. C. Hamakiotes and S. A. Berger, Periodic flows through curved tubes: the effect of the frequency parameter, *J. Fluid Mech.* **210**, 353–370 (1990).
15. S. Tada, S. Oshima and R. Yamane, Flow patterns of the fully developed pulsatile flow in a curved pipe, *Trans. J.S.M.E.* **56**(531), 3240–3247 (1990) (in Japanese).
16. H. A. Simon, M. H. Chang and J. C. F. Chow, Heat transfer in curved tubes with pulsatile, fully developed, laminar flows, *J. Heat Transfer* **99**, 590–595 (1977).
17. N. J. Rabadi, J. C. F. Chow and H. A. Simon, Heat transfer in curved tubes with pulsating flow, *Int. J. Heat Mass Transfer* **25**, 195–203 (1982).
18. W. Y. Soh and S. A. Berger, Fully developed flow in a curved pipe of arbitrary curvature ratio, *Int. J. Numer. Methods Fluids* **7**, 733–755 (1987).
19. A. J. Chorin, A numerical method for solving incompressible viscous flow problems, *J. Comp. Phys.* **2**, 12 (1967).
20. K. A. Hoffmann, *Computational Fluid Dynamics for Engineers*, Vol. 13. EES, Austin, Texas (1989).
21. T. Takami, K. Sudou and K. Sumida, Pulsating flow in curved pipes (1st Report, numerical and approximate analysis), *Bulletin of J.S.M.E.* **27**(234), 2706–2713 (1984).
22. M. Sumida and K. Sudou, Pulsating flow in curved pipes (3rd Report, axial velocity profiles), *Bulletin of J.S.M.E.* **29**(256), 3334–3340 (1986).
23. C. E. Kalb and J. D. Seader, Heat and mass transfer phenomena for viscous flow in curved circular tubes, *Int. J. Heat Mass Transfer* **15**, 801–817 (1972).
24. M. Faghri, K. Javdani and A. Faghri, Heat transfer with laminar pulsating flow in a pipe, *Lett. Heat Mass Transfer* **6**, 259–270 (1979).